Intracluster superelastic scattering via sequential photodissociation in small HI clusters

D. Chastaing, J. Underwood, and C. Wittig[a]
Department of Chemistry, University of Southern California, Los Angeles, California 90089

The photodissociation of expansion-cooled HI monomer by using 266 nm radiation yields H atoms having 12 830 and 5287 cm^{-1} of translational energy in the HI center-of-mass system for the $I(^2P_{3/2})$ and $I(^2P_{1/2})$ [i.e., I and I*, respectively] co-fragments. Irradiating HI clusters [i.e., $(HI)_n$, with $n=2$ being the dominant cluster] with 266 nm radiation produces, among other things, some H atoms whose translational energies are peaked at 20 285 cm^{-1}, which is 7455 cm^{-1} higher in energy than the more energetic of the monomer peaks. These very fast H atoms arise from sequential photodissociation within the clusters. Namely, a weakly bound $I^* \cdot (HI)_{n-1}$ complex is first created by the photodissociation of an HI moiety within $(HI)_n$, and then the photodissociation of a second HI moiety [within $I^* \cdot (HI)_{n-1}$] produces a fast H atom that scatters from the nearby I*, in some cases deactivating it in the process. Thus, the latter superelastically scattered H atom acquires, as translational energy, nearly all of the I* energy (7603 cm^{-1}). For example, for the dimer, the first dissociation event, $(HI)_2 + h\nu \rightarrow H + I(I^*) \cdot HI$, is followed by $I^* \cdot HI + h\nu \rightarrow H_{superelastic} + I–I$. High quality potentials for the relevant HI excited states have been calculated recently, and coupling between $^3\Pi_{0^+}$ (which correlates with I*) and $^1\Pi$ (which correlates with I) has been shown to be due to spin–rotation interaction. There is a high degree of separability between the photodissociation of the second HI moiety and the subsequent H+I* scattering (within a given cluster). This is due mainly to the shape of the $^3\Pi_{0^+}$ potential; specifically, it has a shallow well that persists to small r. The shape of the $^3\Pi_{0^+}$ potential is influenced by relativity; i.e., strong spin–orbit coupling maintains the I* spherical electron density to relatively small r. The $^3\Pi_{0^+} \rightarrow {}^1\Pi$ transition probabilities are calculated for H+I* collisions having different values of the collisional orbital angular momentum quantum number, l, by scaling the spin–rotation matrix elements by $[l(l+1)]^{1/2}$ and using the Landau–Zener model to treat the electronically nonadiabatic dynamics. It is shown that large l values ($l_{max}=52$) play a dominant role in the quenching of I* by H. For example, the partial superelastic scattering cross section is six orders of magnitude larger for $l=52$ than for $l=1$, underscoring the dramatic role of angular momentum in this system. It is noted that HI photodissociation (which is dominated by low l) proceeds almost entirely along the diabats with little transfer of flux between them, whereas H+I* intracluster "collisions" take place with sufficiently large l to facilitate the electronically nonadiabatic process. © *2003 American Institute of Physics.* [DOI: 10.1063/1.1574014]

INTRODUCTION

Understanding the bonding, potential energy surfaces (PES's), and photochemistries of molecules in which relativistic effects (i.e., mass-velocity, Darwin, and spin–orbit coupling) play important roles continues to advance as an area of intellectual and technological importance.[1–13] For example, it is now clear that failure to include such effects in theoretical treatments of systems that contain heavy atoms can compromise seriously the value of such exercises, even at qualitative levels.[2,14,15]

Small molecules that display large relativistic effects can serve as benchmarks against which theoretical models are judged, with HI being a particularly straightforward example. Namely, high level calculations are now able to reconcile, with good accuracy, the experimentally determined

low-lying excited electronic states and photodissociation pathways, including wavelength dependent anisotropies and the branching ratio of the product I-atom spin–orbit levels.[2,3] In general, electronically nonadiabatic transitions can influence reaction pathways and product excitations in photodissociation as well as the corresponding collisional processes. Indeed, understanding the quenching of spin–orbit excitation in atomic collisions is challenging to both theoreticians and experimentalists.[16–25]

An aspect that is not present in lighter systems involves the I-atom excited spin–orbit level, $^2P_{1/2}$, whose electron density is spherical.[26] Because the spin–orbit energy is large (i.e., 7603 cm^{-1}),[27] the $^2P_{1/2}$ spherical electron density remains reasonably robust down to short H–I distances, i.e., relative to light halogens. Consequently, the $I(^2P_{1/2})$ atom couples weakly with the H atom, resulting in a shallow van der Waals-type minimum. Said differently, strong spin–orbit coupling inhibits the participation of "traditional" bonding
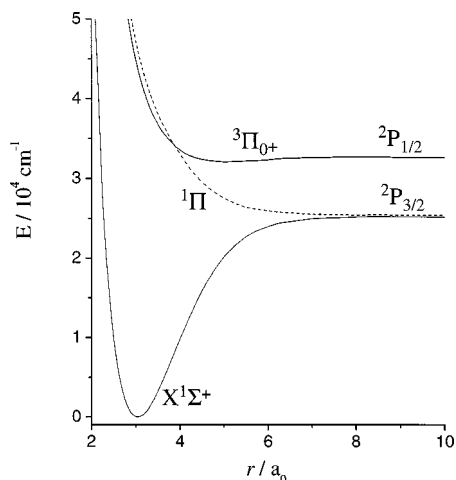
FIG. 1. Potential energy curves for the ground and two low-lying excited electronic states of HI, adapted from Fig. 4 of Ref. 2. The potentials of interest in the current study, $^3\Pi_{0+}$ and $^1\Pi$, cross at $r_c = 3.89$ a.u. and are coupled via spin–rotation interaction. A number of other excited (repulsive) potentials are not shown.
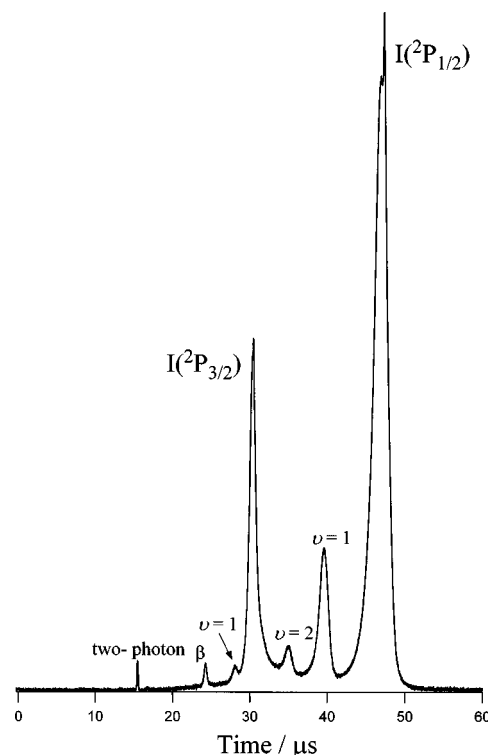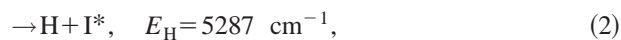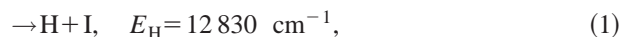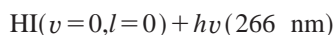

FIG. 2. Time-of-flight spectrum recorded by using a mixture of 4% HI in Ar. The photolysis laser is vertically polarized (see Fig. 3) with an energy of 35 mJ. The time delay between the photolysis and the detection lasers is 40 ns, and 7000 individual traces were summed. Two prominent peaks correspond to the atomic iodine $^2P_{3/2}$ and $^2P_{1/2}$ spin–orbit levels. A small amount of two-photon excitation of HI monomer yields fast hydrogen atoms. (i.e., 3.5 and 3.2×10^6 cm s^{-1}). Peaks labeled $v = 1$ and $v = 2$ are associated with clusters (Ref. 31). Note the β peak, which corresponds to superelastically scattered H atoms.

and antibonding molecular orbitals. This and other relativistic effects have been revealed in the high-level *ab initio* calculations of Alekseyev *et al.*[2,3] for the ground and low-lying HI electronic states, as indicated in Fig. 1. The $X\,^1\Sigma^+$, $^3\Pi_{2,1,0^-}$, and $^1\Pi$ states all correlate with $H + I(^2P_{3/2})$, while $^3\Pi_{0^+}$ and $^3\Sigma^+_{1,0^-}$ correlate with $H + I(^2P_{1/2})$. Hereafter, $I(^2P_{3/2})$ and $I(^2P_{1/2})$ will be referred to as I and I*, respectively.

In general, large product spin–orbit splittings can lead to interesting spectral features, as has been reported for H_2Te,[13] which is isoelectronic with HI. With H_2Te, a long-wavelength tail has been noted in the ultraviolet absorption spectrum, which extends to 400 nm, with apparent vibrational structure at the longest wavelengths. Photodissociation in this spectral region favors the TeH $^2\Pi_{1/2}$ excited spin–orbit level, providing a tunable photolytic source of reasonably monoenergetic H atoms at energies below 2000 cm^{-1}. The relativistic effect in this system provides access to excited PES's at energies that are close to that of the TeH($^2\Pi_{1/2}$) large-r asymptote. There is no counterpart with light systems, where product spin–orbit levels are separated by relatively small energies.

The curves shown in Fig. 1 are relevant to collisions. Namely, the deactivation of I* brought about by a sufficiently energetic H + I* collision occurs via a transition between the $^3\Pi_{0+}$ and $^1\Pi$ diabatic curves. Coupling is due to spin–rotation interaction, and transition probabilities can be estimated by using the Landau–Zener model.[16,28–30] For example, it has been shown to play only a minor role in the photodissociation of HI(l), where l is the rotational quantum number, for l values as high as 10.

Extending the photophysics of gaseous HI to its small (i.e., mainly binary)[31] clusters has yielded interesting results, including a report of "superelastic" scattering, in which a fast H atom produced by HI photodissociation deactivates I*, thereby gaining translational energy. The superelastic peak is shifted by 7455 cm^{-1} (which is 148 cm^{-1} less than the energy of the $^2P_{1/2}$ excited state, 7603 cm^{-1}) from the H

atom peak at 12 830 cm^{-1} that derives from the photodissociation of gas phase HI in its lowest quantum level:

$$HI(v=0, l=0) + h\nu(266 \text{ nm})$$

$$\rightarrow H + I, \quad E_H = 12\,830 \text{ cm}^{-1}, \tag{1}$$

$$\rightarrow H + I^*, \quad E_H = 5287 \text{ cm}^{-1}, \tag{2}$$

where E_H denotes the translational energy of the H atom in the HI center-of-mass (c.m.) system, i.e., $E_H = (127/128)E_{c.m.}$ where $E_{c.m.}$ is the total translational energy in the HI c.m. system. Note that the $E_{c.m.}$ values for reactions (1) and (2) are 12 931 and 5328 cm^{-1}, respectively. As shown in Fig. 2, because the superelastic peak is shifted to a significantly higher energy than all of the other peaks (except one that is due to two-photon excitation of HI)[31] in the spectrum obtained with a particular laser polarization, it can be detected without difficulty, even when it comprises only a small fraction of the H-atom products. Thus, it can serve as a probe of the electronically nonadiabatic process that accounts for the "super" in superelastic.

The analysis presented in this paper enables us to evaluate the respective roles of two possible origins of the observed effect, namely, gas phase scattering versus intracluster scattering with $I^*(HI)_{n-1}$ (see below). Gas phase scattering refers to the photodissociation of HI in the molecular beam

followed by a gas phase collision between a fast H atom and I*, both of which are nascent photoproducts:

$$H(E_H = 12\,830 \ cm^{-1}) + I^* \rightarrow H_{se} + I \qquad (3)$$
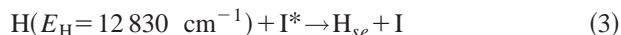
where the subscript se indicates that superelastic scattering has occurred via the deactivation of I*. The translational energy of H_{se} is higher than $E_H = 12\,830 \ cm^{-1}$ by slightly less than the I atom spin–orbit splitting, the difference arising from small kinematic effects in which the I atom gains translational energy.[31–33] A similar process can occur with H atoms having $E_H = 5287 \ cm^{-1}$, i.e., deriving from reaction (2). In this case, however, the superelastic peak is obscured by the more intense signals that are due to reaction (1), as well as the photolysis of $HI(v \geq 0, J)$ molecules that derive from intracluster scattering (see Fig. 2).[31,34] For example, the $I(^2P_{1/2}) v = 3$ contribution is present as a shoulder on the peak labeled $^2P_{3/2}$. (Note that deuterated samples yield a clear $v = 3$ peak.[31])

The intracluster scattering that gives rise to $HI(v)$ is best described as a frustrated attempt at reaction, in which an H atom approaches the I atom in HI with HIH angles of ~90°. Though exchange does not occur (too large a barrier), the ''spectator'' H atom moves because the system gets close to the transition state for H-atom exchange.[31]

Photoexcitation of $(HI)_n$

Next, consider photoinitiated processes that take place within a given cluster, $(HI)_n$, where n is the number of HI molecules in the cluster. In this case, photodissociation of one of the clustered HI molecules removes an H atom, leaving I or I* bound to $(HI)_{n-1}$:

$$(HI)_n + hv \rightarrow H + I \cdot (HI)_{n-1} \qquad (4)$$

$$\rightarrow H + I^* \cdot (HI)_{n-1}. \qquad (5)$$
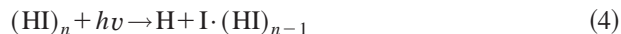
The photolytically produced H atoms can also abstract an H atom from HI, forming H_2. Our experiments are blind to this channel, which is believed to be minor in comparison to reactions (4) and (5).[31,35]

In the discussion that follows, a simple descriptive language is used, in which the I atom is allowed to retain its separate identity, rather than the more formal (and technically correct) description, in which PES's of the iodine$\cdot (HI)_{n-1}$ clusters are used. Because of the large mass difference, the photodissociation of an HI molecule in $(HI)_n$ (for small n values) will leave the resulting I atom bound to the $(HI)_{n-1}$ fragment a high percentage of the time. For example, assume that the H atom escapes without encumbrance. Then, of the 5328 cm^{-1} of c.m. translational energy for the H + I* product channel, approximately 40 cm^{-1} is imparted to the I* atom in the c.m. system of the HI undergoing dissociation. Furthermore, in a binary cluster, this 40 cm^{-1} is shared approximately equally between internal excitation and translational energy of the I* $\cdot$ HI cluster. Because this much internal excitation is significantly less than that required for fragmentation into I* + HI, the clusters indicated in Eqs. (4) and (5) do not dissociate unless I* undergoes deactivation within the cluster. Clusters having $n \geq 3$ will on average acquire more internal energy via intracluster scatter-

ing of the departing H atom than those having $n = 2$. It is unlikely, however, that fragmentation of such clusters constitutes a significant channel under the conditions reported previously[31,34] or here.

Photoexcitation of $I^* \cdot (HI)_{n-1}$

Reaction (5) can be followed by photodissociation of one of the HI molecules within the metastable $I^* \cdot (HI)_{n-1}$ complex, and the H atom thus produced can scatter from the nearby I*, deactivating it in the process:

$$I^* \cdot (HI)_{n-1} + hv \rightarrow H_{se} + remaining \ stuff, \qquad (6)$$

where the vague term *remaining stuff* underscores the complexity of reaction (6). For example, even with the simplest possible metastable cluster [i.e., $I^* \cdot HI$, deriving from the $(HI)_2$ complex] rapid removal of the H atom can place the system on multiple I_2 curves in the region of large iodine–iodine separation.

It is interesting that I* survives while bound to one or more HI molecules long enough to encounter an H atom from subsequent photodissociation, as indicated in Eq. (6). It took us a while to accept this, as it was expected, on the basis of gas phase quenching data,[36] that $I^* \rightarrow I$ relaxation would be too efficient to enable the spin–orbit excited cluster indicated in Eq. (5) to undergo significant photodissociation. We attribute this to strong spin–orbit coupling, which acts to preserve the spherical symmetry of the $^2P_{1/2}$ electron density, the low temperatures of the clusters, and the fact that large photolysis rates that result from high photolysis laser fluences mitigate the $I^* \cdot (HI)_{n-1}$ metastability requirement.

In the material that follows, it will be shown that the gas phase collisional process indicated in Eq. (3) does not play a significant role under the experimental conditions reported here. This implicates species of the form $I^* \cdot (HI)_{n-1}$ as immediate precursors of the observed superelastic scattering. It is not feasible at this point to establish the distribution of n values that participate, though $n = 2$ is believed to dominate.

The strategy used here is to apply knowledge about free HI to the cluster environment. High quality HI potential curves have recently been calculated for several low-lying electronically excited states.[2,3] In particular, the curve crossing that is responsible for the observed superelastic scattering has been examined, and the coupling of these potentials has been attributed to spin–rotation interaction, whose squared matrix elements vary as $l(l+1)$. By combining this coupling mechanism with the Landau–Zener model for surface hopping,[16] it is possible to reconcile the intracluster scattering indicated in Eq. (6), which occurs with a broad range of l values, in contrast to photodissociation of rotationally cold HI, which occurs with only low l values.

EXPERIMENTAL RESULTS

High-n Rydberg time-of-flight (HRTOF) spectroscopy was used to record H-atom TOF distributions (which were then converted to translational energy distributions) following the photolysis of expansion-cooled samples containing HI. The general experimental arrangement shown in Fig. 3 has been described in detail previously.[13,31,37] Briefly, a
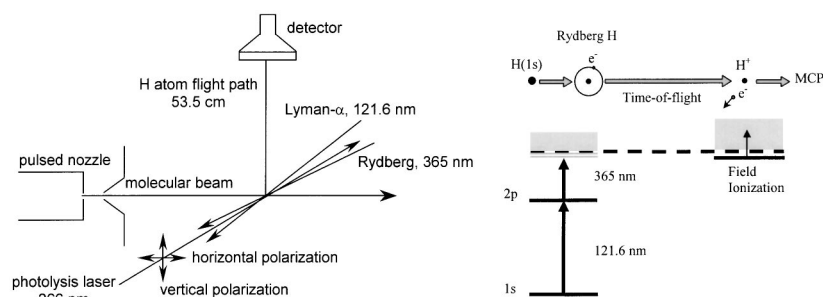
FIG. 3. Schematic of the HRTOF apparatus indicating the polarized 266 nm-photodissociation radiation and the radiations used to create high-n Rydberg H atoms (121.6 and 366 nm). The flight distance is 53.5 cm.

pulsed molecular beam was produced by expanding HI/Ar mixtures into vacuum. The main scattering chamber has a base pressure of $\sim 10^{-7}$ mbar, which is achieved by using a diffusion pump, and contains a quadrupole mass spectrometer (Stanford Research Systems, RGA 300) for monitoring the pulsed molecular beam. The flight tube has a 53.5 cm path length and a 1.5 cm diameter aperture at its entrance; its axis is perpendicular to the molecular beam. In the material presented below, photolysis was carried out by using 266 nm radiation. The two lasers used for the HRTOF measurements will be referred to as the Lyman-α and high-n Rydberg lasers. All three laser beams are focused and overlapped with the molecular beam at the interaction region.

HI number density

Referring to Fig. 3, molecular beams were produced by expanding HI/Ar mixtures (typically 4% HI, with a backing pressure, p_0, of 1 bar) through a 0.8 mm diameter pulsed nozzle, with collimation achieved by using a 1 mm diameter skimmer located 2.0 cm downstream from the nozzle. For a free-jet expansion, the density along the jet axis is given by[38]

$$n(z) = n_0(z_0/z)^2, \tag{7}$$

where $z_0 = ar_0$; $a = 0.80$ for an ideal monatomic gas; r_0 is the nozzle radius; n_0 is the number density at the nozzle; and z is the distance from the nozzle exit plane. At the interaction region, which is 7 cm from the nozzle exit plane, Eq. (7) gives a total HI density [i.e., including that present in the form of $(HI)_n$ clusters] of 2×10^{13} cm^{-3} for 4% HI and $p_0 = 1$ bar. The molecular beam diameter at the interaction region is ~ 3 mm.

Photoexcitation

Photolysis was achieved by using the 266 nm fourth harmonic of a Nd:YAG laser (Continuum 9010), which provided 266 nm energies up to 45 mJ. The HI absorption cross section at 266 nm, σ_{abs}^{266} is 2×10^{-19} cm^2,[39] which is sufficient to bring about a high degree of photodissociation. For example, for a photolysis beam diameter of ~ 1 mm, a 40 mJ pulse corresponds to a fluence, Φ, of $\sim 10^{19}$ photons cm^{-2}, in which case the product $\sigma_{abs}^{266} \times \Phi$ has a value of ~ 2, suggesting efficient photodissociation.[40] This was confirmed experimentally. Namely, the HRTOF signal amplitudes varied weakly with photolysis laser energy in this regime.

In addition, the efficiencies of the Lyman-α and high-n Rydberg excitation steps should be considered. Lyman-α radiation was generated by frequency tripling in Kr. The output

of a dye laser (Continuum ND 6000) pumped by the 532 nm output of a Nd:YAG laser (Continuum PL 8000) and operating with LDS 750 dye in methanol was doubled after passing through an autotracker (Inrad), yielding ~ 14 mJ at 364.8 nm. This beam was focused into the tripling cell. The high-n Rydberg step was realized by using ~ 7 mJ in the region 365.2–365.3 nm (0.16 cm^{-1} linewidth), which was generated by using a laser system that is similar to the one used to generate Lyman-α radiation.

It has not been possible for us to estimate, with reasonable accuracy, the efficiencies of the Lyman-α and high-n Rydberg photoexcitation steps for two main reasons. First, the generation of the Lyman-α radiation is controlled by many properties of the tripling process. For example, it depends on laser parameters (power, spatial mode, and linewidth), the cell pressure (e.g., its effect on phase matching), and the focusing arrangement, which is located inside the molecular beam chamber. Second, it is difficult to estimate the efficiency of high-n Rydberg photoexcitation. This step is carried out in a weak dc electric field that eliminates the usual $\Delta L = \pm 1$ angular momentum optical selection rule, by making space anisotropic for the weakly bound high-n levels.[41] This enables large L values to be prepared, thereby providing the needed metastability of the high-n Rydberg H atoms as they drift with their nascent velocities through the field-free time-of-flight region to the microchannel plate detector, where they are field ionized and detected.

These ambiguities notwithstanding, several facts can be enlisted to establish an upper bound to the efficiency of the combined Lyman-α and high-n Rydberg steps: (i) Four-wave mixing is known to yield significantly higher 121.6 nm energies than the frequency tripling in Kr used in the present study.[42,43] This results in correspondingly higher HRTOF detection sensitivities, indicating that we are currently operating with 121.6 nm fluences that are well below those needed to saturate the Lyman-α transitions. (ii) We have obtained larger signals by fine-tuning the Lyman-α and Rydberg steps, confirming the lack of saturation in both steps. (iii) The complete, simultaneous saturation of both steps would result in the transfer of 1/3 of the ground state population to high-n. Taking these factors into account, an upper bound of 10^{-3} is assigned to the probability that the H atoms traveling toward the detector are promoted from the ground state to a metastable high-n, high-L Rydberg level. This is believed to be a safe upper bound.

The experimental TOF spectra, $f_{tof}(t)$, were converted to H atom translational energy spectra, $g(E_H)$, by using the following relations, in which the correction for the velocity
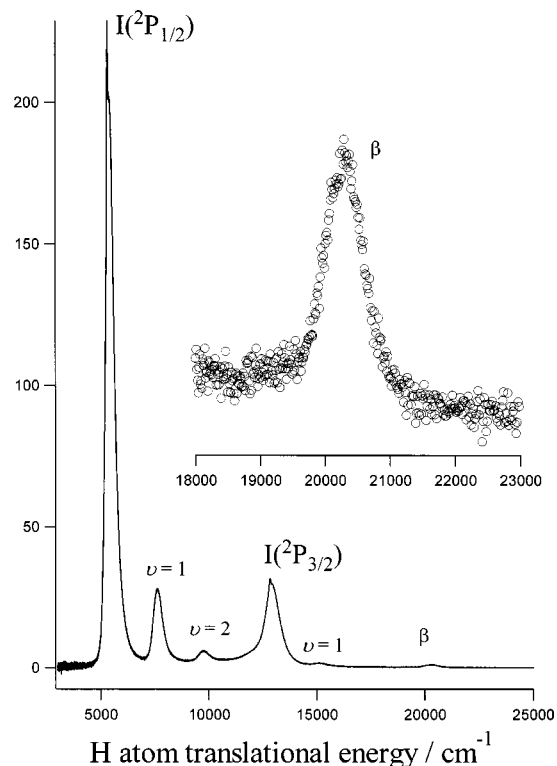
FIG. 4. H-atom translational energy spectrum obtained with the photolysis laser vertically polarized and an energy of 35 mJ (4% HI in Ar). The delay between the photolysis and the detection lasers is 40 ns. Peaks labeled $v=1$ and $v=2$ derive from photoinitiated intracluster scattering; their energies are offset from the monomer peaks by approximately the HI(v) vibrational energies. Specifically, photodissociation of a clustered HI molecule liberates an H atom that encounters another HI molecule. This interaction yields HI(v); see text for details. Expanding the vertical scale between 18 000 and 23 000 cm^{-1} highlights the β peak which is shifted from the $^2P_{3/2}$ monomer peak by almost the iodine spin–orbit energy.

of the molecular beam in the laboratory frame is taken into account:

$$E_H = (m_H/2)[(d_{tof}/t)^2 + v_{mb}^2], \tag{8}$$

$$g(E_H) \propto t^3 f_{tof}(t), \tag{9}$$

where v_{mb} is the speed of the molecular beam and d_{tof} is the length of the flight path.

Figures 4 and 5 show H-atom translational energy distributions obtained in the regime of efficient photolysis, i.e., by using 35 mJ at 266 nm. With 4% HI, there is sufficient clustering that prominent features are present that are due to the photodissociation of the HI(v,J) molecules that derive from photoinitiated intracluster scattering. The well-isolated β peak (centered at 20 285 cm^{-1}) obtained by using vertical polarization (see Fig. 3) is blue-shifted by 7455 cm^{-1} from the peak that is due to the I channel of HI monomer photodissociation.

Gas phase superelastic scattering: $H + I^* \rightarrow H_{se} + I$

Consider gas phase collisions that take place in the molecular beam between I* and the fast H atoms (H_{fast}) that are associated with an I co-fragment, i.e., those having $E_H = 12\,830$ cm^{-1}. Specifically, can the resulting deactivation

of I* account for the superelastic peak, which, after all, is a minor channel in the overall photochemistry?

The time rate of change of the H_{se} density [H_{se}], via these collisions is given by the expression

$$(d/dt)[H_{se}] = k_{na}[H_{fast}][I^*], \tag{10}$$

where the rate coefficient for the nonadiabatic process, k_{na}, can be expressed as

$$k_{na} = v \sum_l \sigma_{na}(l) \tag{11}$$

$$= v \sigma_{na}^{tot}, \tag{12}$$

where $\sigma_{na}(l)$ is the partial cross section for a collision having orbital angular momentum quantum number l, and v is the magnitude of the initial relative velocity, which in this case is equal to 1.7×10^6 cm s^{-1}. The physics of the collisional process is manifest in the $\sigma_{na}(l)$, as discussed below. A value of 3×10^{-17} cm^2 is now introduced *ad hoc* for the total cross section, σ_{na}^{tot}, yielding $k_{na} = 5.1 \times 10^{-11}$ cm^3 s^{-1}. This will be used below in several estimates, and we will then return to a discussion of the $\sigma_{na}(l)$. Scaling as per different σ_{na}^{tot} values is trivial.

For a photodissociation efficiency of γ and branching fractions F_I and F_{I^*} for the I and I* channels, respectively, [H_{se}] at short delay times following the photolysis pulse is given by

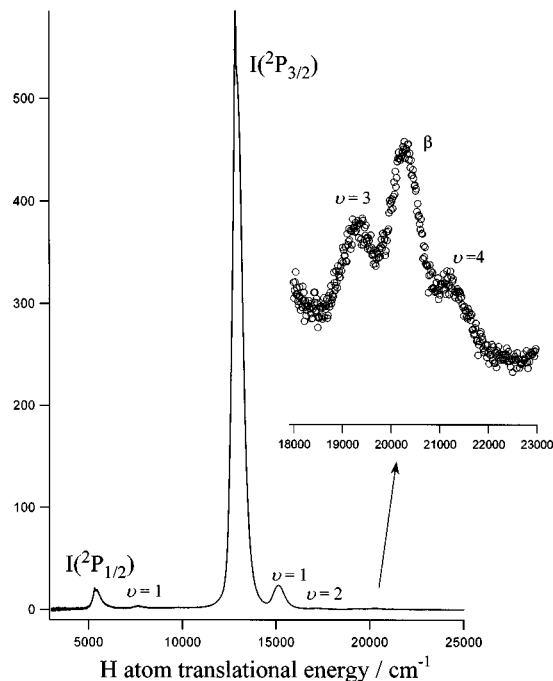$$[H_{se}] = k_{na}\gamma^2 F_I F_{I^*}[HI]^2 \Delta t, \tag{13}$$

FIG. 5. Translational energy spectrum obtained under the same conditions as in Fig. 4, but with the photolysis laser horizontally polarized. Note that the shape and intensity of the β peak is affected little by the photolysis laser polarization.
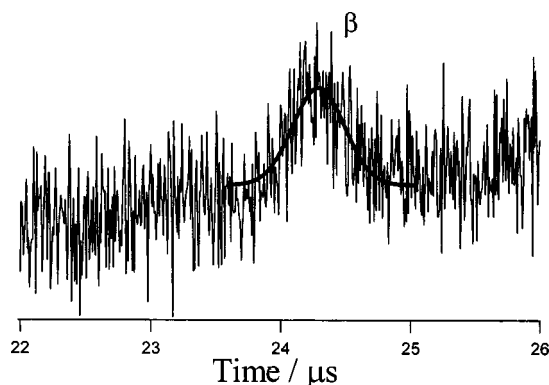
FIG. 6. Trace showing part of the time-of-flight spectrum around the β peak (4% HI in Ar, photolysis laser vertically polarized, 4 mJ). The time delay between the photolysis and the detection lasers is 30 ns. The spectrum is the sum of 5000 individual traces. Even with a photolysis laser energy as low as 4 mJ, and despite the low S/N, the β peak is still observable.

where Δt is the time delay between the photodissociation and probe pulses. Equation (13) is premised on Δt being much smaller than the characteristic times for the production and removal of $[\mathrm{H}_{se}]$.

As mentioned above, for the highest photolysis laser energies used in the present experiments (i.e., 35 mJ), photodissociation is efficient. Because comparisons will be made, however, to data recorded by using a photolysis laser energy of 4 mJ (Fig. 6), a value of $\gamma=0.1$ is introduced. With $F_\mathrm{I}=0.62$ and $F_{\mathrm{I}*}=0.38$,[44] $[\mathrm{HI}]=2\times10^{13}$ cm^{-3}, and $k_{na}=5.1\times10^{-11}$ cm^3 s^{-1}, Eq. (13) yields

$$[\mathrm{H}_{se}]=4.8\times10^{13}\Delta t. \qquad (14)$$

Thus, for $\Delta t=30$ ns, this estimate gives $[\mathrm{H}_{se}]=1.4\times10^6$ cm^{-3}. The effective volume is defined as the overlap region of the three laser beams and the molecular beam. The interaction volume is estimated to be ~1 mm^3, and the number of H_{se} atoms in this volume is ~1400. The 30 ns delay serves to lessen the requirement that the beams are perfectly overlapped in the interaction volume (which turns out to be quite difficult to achieve), because the fast H atoms [i.e., $E_\mathrm{H}=12\,830$ cm^{-1}, see Eq. (1)] travel 0.5 mm in 30 ns, thus smearing out spatial inhomogeneities brought about by imperfect overlap.

The fraction of the (isotropically scattered) H_{se} atoms that reach the detector (i.e., the area of the detector divided by the area of a sphere whose radius is the flight path) is 1.7×10^{-3}. Combining this with the number of H_{se} atoms in the interaction volume (~1400) and the upper bound of 10^{-3} for the efficiency of the combined Lyman-α and high-n Rydberg steps, it is concluded that the β peak would contribute a maximum of $\sim2\times10^{-3}$ counts per laser firing, were it due solely to gas phase superelastic scattering.

The β peak shown in Fig. 6 is the result of averaging 5000 spectra, and an analysis of the signal indicates that a minimum of 10^2 counts are contained in this feature. Thus, we conclude that the signal shown in Fig. 6, despite its low S/N, is too large to be the result of gas phase superelastic scattering.

An alternate (and more compelling) way to set a limit on the degree of participation of gas phase superelastic scatter-

ing uses the experimentally determined ratio $[\mathrm{H}_{se}]/[\mathrm{H}_{\mathrm{total}}]$. This fraction is obtained by comparing the area of the superelastic feature to the area of all of the other features, taking into account the spatially anisotropic nature of the H-atom recoil directions from HI monomer photodissociation (Figs. 4 and 5). The ratio $[\mathrm{H}_{se}]/[\mathrm{H}_{\mathrm{total}}]$ was found to increase by an order of magnitude (10^{-3} to 10^{-2}) as the 266 nm energy increased from 4 to 35 mJ. Thus, over the range of 266 nm fluences used in the present study, 10^{-3}–10^{-2} of the H atoms undergo superelastic scattering.

The $\sigma_{na}^{\mathrm{tot}}$ value introduced above of 3×10^{-17} cm^2 corresponds to a small fraction of the gas phase H atoms undergoing superelastic scattering in 30 ns, namely, the order of one part in 10^6. Even with the unreasonably large parameter values $\gamma=1$ and $\sigma_{na}^{\mathrm{tot}}=3\times10^{-16}$ cm^2, the resulting $[\mathrm{H}_{se}]$ value obtained by using Eq. (13) is still three orders of magnitude smaller than $[\mathrm{H}_{\mathrm{total}}]$.

On the basis of the above considerations, it is concluded that the β peaks shown in Figs. 2, 4, 5, and 6 are the result of "intracluster collisions" rather than gas phase bimolecular collisions involving unclustered atoms.

DISCUSSION

Though photoinitiated intracluster processes differ in several respects from their gas phase counterparts, the basic character of the corresponding gas phase process in general is retained. In the case under consideration, it will be shown that there is an unusually high degree of separation between photodissociation and subsequent H+I* scattering. Thus, we shall begin with a discussion of H+I* gas phase collisions.

Referring to Fig. 1, it has been pointed out by Balakrishnan *et al.*[3] that the $^3\Pi_{0^+}$ and $^1\Pi$ diabatic potentials interact at their crossing region only via spin–rotation interaction.[45] Furthermore, these authors have pointed out that this coupling plays a negligible role in the photodissociation of rotationally cold HI, with dissociation proceeding almost entirely on the $^3\Pi_{0^+}$, $^1\Pi$, and $^3\Pi_1$ diabats, the latter of which does not cross either $^3\Pi_{0^+}$ or $^1\Pi$. They estimated a coupling matrix element in the region of the $^3\Pi_{0^+}/^1\Pi$ crossing point ($r_c=2.06$ Å) of $\mathrm{H}_{sr}=2.67$ cm^{-1} for $l=1$, where l is either the rotational quantum number or, as discussed below, the collisional orbital angular momentum quantum number. For other values of l, this matrix element scales as $[l(l+1)]^{1/2}$.

Transition probabilities between the $^3\Pi_{0^+}$ and $^1\Pi$ diabats can be estimated by using the Landau–Zener formula[16]

$$P(l)=\exp\{-2\pi|\mathrm{H}_{sr}(l)|^2/\hbar v_{\mathrm{rad}}(l)\Delta F\}, \qquad (15)$$

where $P(l)$ is the probability, for a given value of l, that a transition takes place between the *adiabats* (see Fig. 7), $\mathrm{H}_{sr}(l)$ is the l-dependent spin–rotation coupling matrix element, $v_{\mathrm{rad}}(l)$ is the magnitude of the radial component of the relative velocity at the crossing point, r_c, and ΔF is the magnitude of the difference between the slopes of the $^1\Pi$ and $^3\Pi_{0^+}$ potentials at r_c. Note that centrifugal terms in the effective potentials do not affect ΔF.

The probability that the *adiabatic paths are followed* is $1-P(l)$, which is equal to 0.8×10^{-5} for $l=1$ [i.e., using Eq. (15) with $\mathrm{H}_{sr}=2.67$ cm^{-1}, $v_{\mathrm{rad}}(l=1)=1.7\times10^4$ ms^{-1},
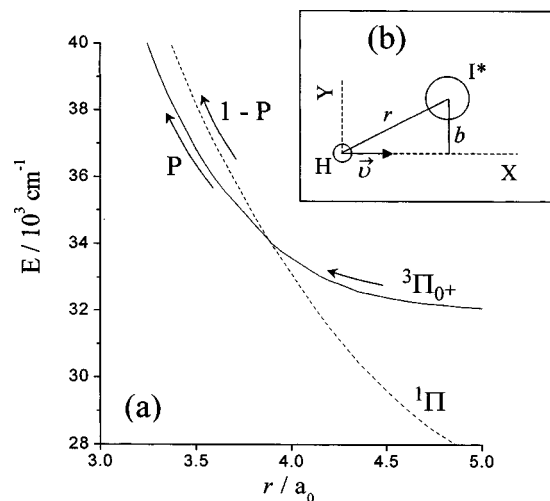
FIG. 7. (a) Diagram showing the $^1\Pi$ (---) and $^3\Pi_{0+}$ (—) HI diabats. The probability, P, to stay on $^3\Pi_{0+}$ (i.e., of a transition taking place between the adiabatic curves that arise from coupling $^1\Pi$ and $^3\Pi_{0+}$ in the crossing region) is given by the Landau–Zener formula. Thus, $1-P$ is the probability of a transition from $^3\Pi_{0+}$ to $^1\Pi$. (b) Schematic diagram of the collision of H with I*. The classical angular momentum is $L=\mu v b$.

and $\Delta F = 6.3 \times 10^3$ cm^{-1} Å^{-1}]. This small probability underscores the diabatic nature of HI photodissociation with rotationally cold samples, where photoexcitation of the $^3\Pi_{0+}$, $^1\Pi$, and $^3\Pi_1$ diabats is carried through to products with negligible transfer of flux among these potentials.

Collisions between H and I*

Referring to Fig. 7, a collision between an H atom and I* that starts on the $^3\Pi_{0+}$ potential can exit on the $^1\Pi$ potential. Though large $P(l)$ values might be anticipated on the basis of the photodissociation results mentioned above, there are important differences between photodissociation and H+I* collisions. For example, with the latter, large values of l are involved. Moreover, it is easy to detect I* deactivation in the form of superelastic scattering, as there is minimal background signal.

The probability, for a given collisional orbital angular momentum whose quantum number is l, that a transition between the $^3\Pi_{0+}$ and $^1\Pi$ curves has occurred after the collision is over is given by

$$\mathbf{P}(l) = 2P(l)[1-P(l)], \quad (16)$$

where $\mathbf{P}(l)$ is the net probability that an electronically nonadiabatic transition has occurred as a result of r having crossed r_c twice—initially on the incoming trajectory and again on the outgoing trajectory. As pointed out above, in each of these crossings, the diabatic pathways are favored as long as $P(l)$ is of order unity, which is overwhelmingly the case for small values of l. Note that if a trajectory follows a diabat on both the incoming and outgoing paths, the net effect is electronic adiabaticity. Nonadiabaticity occurs because propagation through the crossing region twice (i.e., incoming and outgoing trajectories) follows a diabat one time and follows an adiabat the other time.

The partial cross section for a given value of l is given by

$$\sigma_{na}(l) = \mathbf{P}(l) 2\pi[\hbar/\mu v]^2 l, \quad (17)$$

where μ is the reduced mass and v is the speed of an H atom having $E_H = 12\,830$ cm^{-1}. As mentioned above, unlike the photodissociation of rotationally cold HI, large values of l are involved in the collisions. For example, an impact parameter of 1 Å and $E_H = 12\,830$ cm^{-1} corresponds to $l=28$, and because $H_{sr}(l)$ is proportional to $[l(l+1)]^{1/2}$, $\mathbf{P}(l)$ increases from 1.6×10^{-5} to 7.7×10^{-3} as l increases from 1 to 28. Thus, spin–rotation interaction is more important for energetic collisions, such as those considered here, than for the photodissociation of rotationally cold molecules at the same total energy.

Trajectories

Classical trajectory calculations for H+I* inelastic scattering on the potentials of interest (i.e., $^3\Pi_{0+}$ and $^1\Pi$) have been carried out for different values of the impact parameter, b. The goal was to calculate the distribution of H-atom translational energies deriving from the collisional quenching of I* by H, and to compare this to the experimental superelastic peak. The justification for using this binary collision model to reconcile results obtained with clusters is given in a later section.

The initial H-atom translational energy was 12 830 cm^{-1}, with I* at rest. The equations of motion were integrated numerically by using the fourth-order, single-step Runge–Kutta method.[32,46,47] Trajectories followed $^3\Pi_{0+}$ up to the crossing point, where a transition to $^1\Pi$ was assumed to take place. The trajectory was then continued on $^1\Pi$. Alternatively, trajectories were also calculated in which the $^3\Pi_{0+} \rightarrow {}^1\Pi$ transition was assumed to take place on the way out. The use of classical mechanics is justified because of the high translational energies. Note that total angular momentum is not conserved, as the change in electronic angular momentum is not accounted for by changes in l. This is not problematic for the large l values (~ 50) under consideration. These calculations enable us to obtain, with minimal computing and sufficient accuracy, the general behavior of the nuclear motions (Figs. 8 and 9).

Figures 8(a) and 8(b) show that the maximum l value for which a $^3\Pi_{0+} \rightarrow {}^1\Pi$ transition can occur is 52, corresponding to an impact parameter of 1.9 Å. Figure 8(b) depicts the variation of the H-atom speed throughout the trajectory. For $l \leq 52$, collisions in which I* is quenched via $^3\Pi_{0+} \rightarrow {}^1\Pi$ result in H atoms whose translational energies are increased by *almost* the I-atom spin–orbit splitting, i.e., the I atom gains a small amount of translational energy. The superelastic H atom translational energy as a function of l is given in Fig. 10. It varies from 20 227 cm^{-1} for $l=52$ to 19 797 cm^{-1} for $l=0$, corresponding to an energy spread of 430 cm^{-1}. The maximum calculated value of the H_{se} translational energy is shifted from 12 830 cm^{-1} by 7397 cm^{-1}, which is consistent with the experimental value for the energy difference between the β and monomer peaks (i.e., 7455 cm^{-1}).

From the trajectory calculations, the l-dependent radial velocity at r_c was also determined; thus, it was possible to calculate the Landau–Zener probability as a function of l. Figure 11 gives (i) $1-P(l)$; (ii) $\mathbf{P}(l)$; and (iii) $\sigma_{na}(l)$,
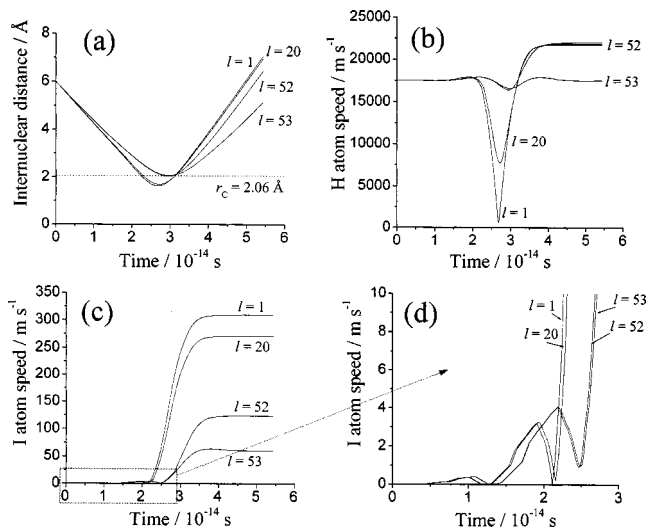
FIG. 8. Trajectory calculations for different values of impact parameter and with the $^3\Pi_{0+}$ to $^1\Pi$ transition occuring on the incoming portion of the trajectory. (a) Internuclear distance H–I. For $l \geqslant 53$, the impact parameter is too large for a transition from $^3\Pi_{0+}$ to $^1\Pi$ to occur. (b) The speed of H remains fairly constant until the trajectory reaches the potential well, as shown by the small bump. For $l \leqslant 52$, a transition from $^3\Pi_{0+}$ to $^1\Pi$ is assumed to take place at r_c, and the trajectory continues on $^1\Pi$. As the system goes through the classical turning point, the H-atom translational energy passes though a minimum. At the end of the trajectory, the hydrogen atom has gained translational energy by almost the spin–orbit splitting of iodine. (c) The iodine atom gains speed. (d) Expanded scales, enable the beginning of the trajectory to be examined. Note the two small bumps that correspond to acceleration and deceleration as the system follows $^3\Pi_{0+}$.

which were obtained by using Eqs. (15)–(17). These functions increase sharply with l, especially for $l \geqslant 50$, where $\sigma_{na}(l)$ varies from 2.6×10^{-18} cm^2 for $l = 50$ to 2.2×10^{-17} cm^2 for $l = 52.7$. This dramatic variation shows that large l are strongly favored for a nonadiabatic transition to occur.

The above procedure yields σ_{na}^{tot} values of $\sim 3 \times 10^{-17}$ cm^2. As discussed earlier, this is still insufficient to rationalize the observations by invoking gas phase scattering.
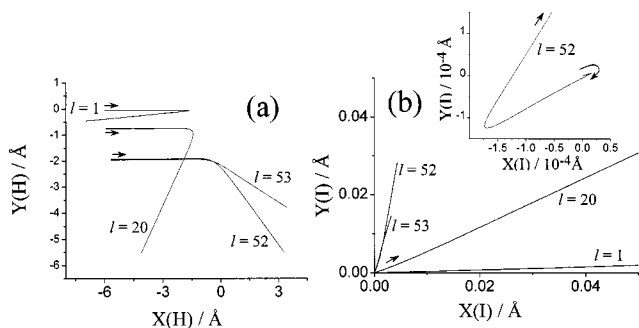

FIG. 9. Cartesian coordinates for (a) the H atom; (b) the iodine atom. Arrows indicate directions of motion. The H atom, whose initial velocity lies along the X axis, approaches I* (which is initially at rest) on $^3\Pi_{0+}$. I* moves ever-so-slightly in response to a small barrier (~ 70 cm^{-1}) centered at $\sim 8\,a_0$. Throughout the attractive part of the shallow well centered at $\sim 5\,a_0$ (~ 600 cm^{-1}), I* moves toward the H atom. Deceleration occurs as r_c is approached, where the $^3\Pi_{0+} \rightarrow {}^1\Pi$ transition occurs. Due to its large mass, the I atom moves very little (e.g., during the $l = 52$ collision, the H atom travels 10 Å while the I atom travels only 0.03 Å).
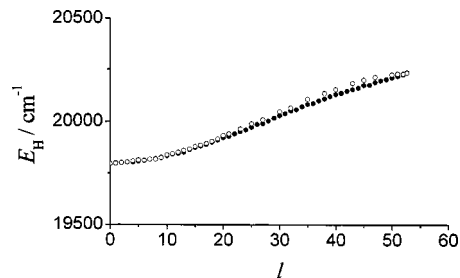

FIG. 10. H-atom translational energy as a function of the orbital angular momentum quantum number l. The transition from $^3\Pi_{0+}$ to $^1\Pi$ occurs on (●) incoming trajectories; (○) outgoing trajectories. For $l \geqslant 53$, the crossing at r_c is not reached.

Referring to Figs. 10 and 11, the partial cross sections, $\sigma_{na}(l)$, can be converted to the energy domain by using the Jacobian dl/dE. The shape of $\sigma_{na}(E)$ is similar to that of $\sigma_{na}(l)$: it rises monotonically from 19 797 to 20 100 cm^{-1}, and then increases more sharply up to 20 227 cm^{-1}. The large values of l, for which the cross section is maximum, correspond to the largest values of H$_{se}$ translational energies (i.e., 20 227 cm^{-1} for $l = 52$). This is consistent with the experimental result that places the center of the superelastic peak at 20 285 cm^{-1}, with a full-width-at-half-maximum (FWHM) of ~ 700 cm^{-1}. This is also consistent with the 430 cm^{-1} spread in energy found from the trajectory calculations, considering that the broadening of the observed β peak includes the resolution of the experimental apparatus.

Intracluster scattering

Intracluster processes figure prominently in the distributions shown in Figs. 4 and 5. Namely, features are readily identified as arising from the photodissociation of the HI(v,J) product that is believed to derive from nonreactive H + HI encounters following the photodissociation of an HI molecule within (HI)$_n$.[48] The case in which the $n = 2$ contribution dominates over contributions arising from $n > 2$ has been examined in detail.[31]

In the study reported here, the cluster size distribution (i.e., [(HI)$_n$] versus n at the interaction region 7 cm downstream from the nozzle) is assumed to be a monotonically decreasing function of n. It depends on the HI concentration
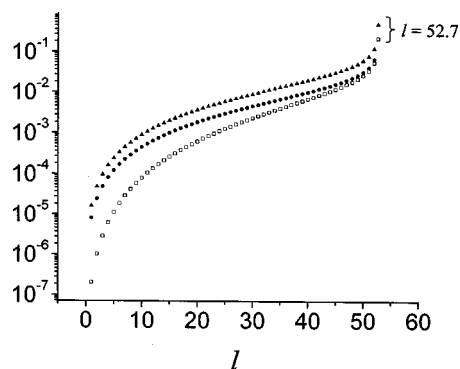

FIG. 11. Filled circles, $1 - P(l)$; filled triangles, $P(l)$; open squares, $\sigma_{na}(l)$ in Å^2. Equation (16) indicates that $P(l)$ has a maximum of 0.5. This occurs for the noninteger value $l = 52.7$.
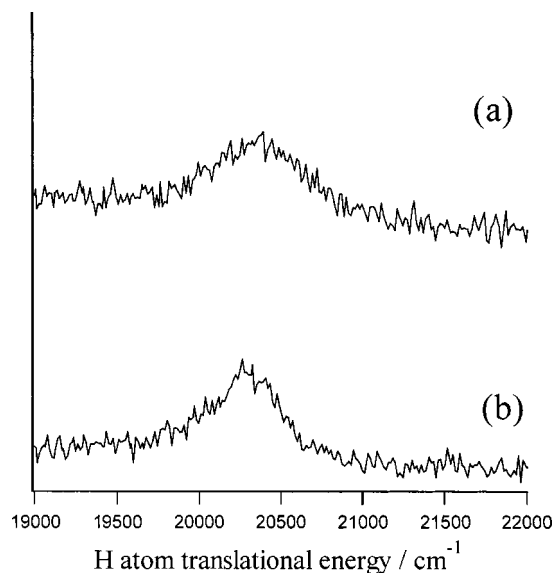
FIG. 12. Translational energy spectra showing the β peak. The photolysis laser is horizontally polarized with an energy of 13 mJ. The time delay between the photolysis and detection lasers is 30 ns. (a) 4% HI in Ar; (b) 2% HI in Ar. Differences are modest.

in the expansion, as well as the time delay between the opening of the pulsed valve and the introduction of the 266 nm photolysis pulse.[31] The features due to HI(v,J) (see Figs. 4 and 5) are essentially identical to those reported earlier under conditions of minimal clustering.[31]

Though the β feature can, in principle, contain significant contributions from several values of n, there was no discernible change in the shape of this feature in going from 4% to 2% HI, or in going from an Ar carrier to a He carrier, while optimizing the signal with respect to the aforementioned delay time, as indicated in Fig. 12. Only the signal amplitude decreased (by as much as an order of magnitude). In addition, as mentioned above, data taken under conditions of *far less* clustering,[31] in which $n=2$ is believed to dominate over all higher n combined, show no differences other than smaller amplitudes of the signals that arise from clusters. Thus, it is concluded that the β peak is due primarily to small clusters, with $n=2$ being the largest contributor. The sharpness of the peak and the fact that it lies 7455 cm^{-1} above $E_H=12\,830$ cm^{-1} (i.e., nearly the I* spin–orbit energy above $E_H=12\,830$ cm^{-1}) suggests a single scattering event that involves a departing H atom and I*.

The calculations whose results are summarized in Fig. 8 are for gas phase collisions. Cluster environments are, in general, more complicated, and comparisons between the computed results and the experimental results obtained with (HI)$_n$ should be pursued with caution. Several relevant aspects that are germane to the case under consideration are worth noting.

Dimer geometry

Figure 13 shows the L-shaped geometry of the dimer, based on the theoretical estimates of Buckingham and Fowler[49] and Hannachi and Silvi.[50] All binary hydrogen halide complexes (HX–HY) are believed to have this L-shaped
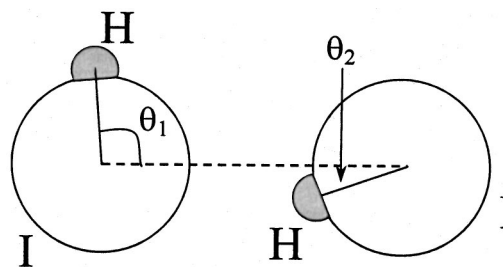

FIG. 13. Theoretical estimates of the (HI)$_2$ equilibrium geometry (Refs. 49 and 50); $\theta_1=94°$, $\theta_2=2°$, and the I–I distance is ~ 5 Å.

geometry; a number have been measured,[51–54] and there is no experimental or theoretical evidence to the contrary. It is known that the H atoms are delocalized significantly as per large zero-point excursions, and thus there is a broad range of angles θ_1 and θ_2. Note that even when starting with (HI)$_3$, the photodissociation of I* $\cdot$ (HI)$_2$ will result in superelastic scattering in which the exiting H atom escapes, in most cases directly into vacuum (i.e., without further scattering) after its interaction with I*.

Referring to Fig. 13, photodissociation of the HI on the right (the *interior* HI) is believed to result in the HI(v,J) product that gives rise to the strong signals labeled as such in Figs. 4 and 5.[31] Photodissociation of the HI on the left (the *exterior* HI) yields I and I*, the latter having a quantum yield of 0.40 at 266 nm.[44] As mentioned earlier, the I* remains bound to its HI partner, because when the exterior HI is photodissociated, the translational energy imparted to the I* in the c.m. system of the exterior HI is approximately 40 cm^{-1}, which is shared equally by translational and internal energies of the I* $\cdot$ HI complex [when (HI)$_2$ is the parent]. The binding energy of the analogous Cl* $\cdot$ HCl complex has been estimated to be ~ 130 cm^{-1},[55] and for the I* $\cdot$ HI system under consideration here, there is no possibility that 20 cm^{-1} of internal excitation is sufficient to cause fragmentation to I* + HI. Thus, the I* $\cdot$ HI complex remains intact with approximately 20 cm^{-1} of internal excitation. As a result of the large degree of H-atom delocalization present in the weakly bound I* $\cdot$ HI complex, some of the H atoms that are photoejected from this complex will interact with I* on the way out. The resulting deactivation of I* accounts for the β peak.

Photodissociation followed by scattering: The case for sequential processes

The iodine–iodine distance in (HI)$_2$ is approximately 5 Å,[50] and, assuming that (HCl)$_2$[35] and Cl* $\cdot$ HCl[51] can be used as analogs, the binding energy of the I* $\cdot$ HI complex is several times smaller than that of (HI)$_2$. Thus, the iodine–iodine distance in I* $\cdot$ HI will be taken to be 5.1 Å, which we believe is a conservative lower bound. The 20 cm^{-1} of internal energy imparted by HI photodissociation within (HI)$_2$, as well as the highly anharmonic PES, also support 5.1 Å as a lower bound. This number has been used to construct diagrams (a)–(c) in Fig. 14, which depict snapshots of the photodissociation of the HI moiety, assuming classical motion for the nuclei. The potentials shown on the bottom are for HI;[2] they do not account for three-body interactions.
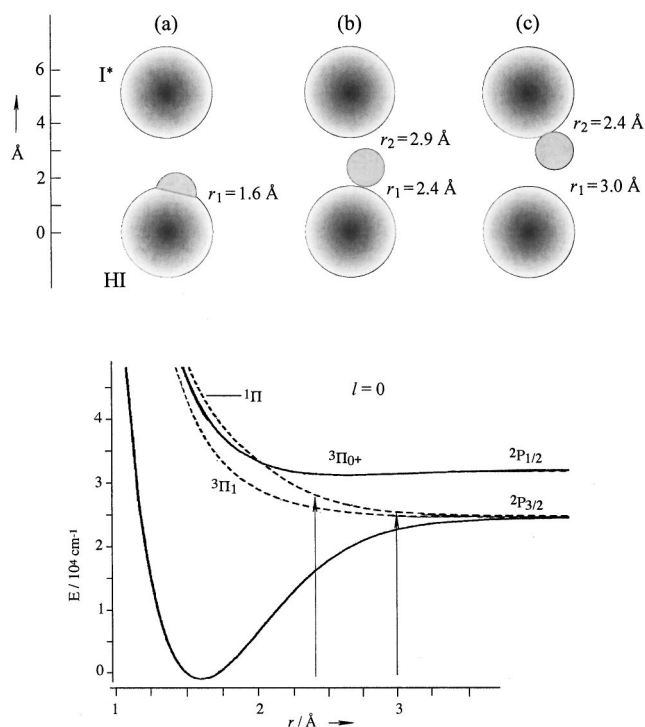
J. Chem. Phys., Vol. 119, No. 2, 8 July 2003

Intracluster superelastic scattering   937

FIG. 14. Schematic diagram of the photodissociation of the HI moiety within the I*·HI complex.

Referring to Fig. 14(b), by the time r_1 has increased to 2.4 Å, the H atom has gained approximately 70% of the translational energy it can acquire via HI photodissociation. The distance between the H atom and I* is still large (2.9 Å), and there is little interaction between these atoms; e.g., note the flatness of the $^3\Pi_{0+}$ potential for $r > 2.2$ Å. The slightly larger electron density on the side of the H atom facing the I* (relative to a free H atom) does not change the H+I* interaction significantly.

Referring to Fig. 14(c), with r_1 now extended to 3.0 Å, there is modest repulsion on $^1\Pi$, and the H atom has developed to a large extent the identity of a free atom. At the same time, r_2 is 2.4 Å, and at this distance the $^3\Pi_{0+}$ potential is very shallow. Even with $r_1 = 3.2$ Å, in which case the $^1\Pi$ potential energy is down to only hundreds of cm^{-1}, the corresponding r_2 value of 2.2 Å is still in a very flat region of $^3\Pi_{0+}$. Thus, the photodissociation and scattering processes are, to a large extent, separable, in the sense that the former proceeds almost to completion before the latter begins.

This near separability is attributed to a relativistic effect: strong spin–orbit interaction in the iodine atom results in a shallow van der Waals-type well on $^3\Pi_{0+}$ that persists to small r. The spherical charge density of I* is anathema to the formation of bonding and antibonding orbitals for $r \gtrsim 2$ Å. Note that H-atom scattering from an adjacent $^2P_{3/2}$ atom would not present nearly as separable a situation for the dynamics, e.g., on the $^1\Pi$ potential shown in Fig. 14.

CONCLUSIONS

It has been shown that collisions within the molecular beam between H and I* atoms whose parentages are not the *same* cluster play an insignificant role. This implicates intra-

cluster scattering as the origin of the superelastic β peak. There is a striking similarity between the β peak and the theoretical results obtained by using the model presented above. On this basis, it is concluded that intracluster superelastic scattering has a great deal in common with the corresponding gas phase process.

Coupling of the $^3\Pi_{0+}$ and $^1\Pi$ diabatic potentials, which occurs near r_c via spin–rotation interaction, is too weak to play a role in the photodissociation of rotationally cold HI, e.g., $H_{sr} = 2.67$ cm^{-1} for $l = 1$. Rather, the photoexcited diabats are followed to products with no significant transfer of flux between them. On the other hand, because H_{sr} scales as $[l(l+1)]^{1/2}$, spin–rotation coupling acquires a privileged status in the energetic H+I* collisions of the kind considered here. For example, the area of the β peak is $\sim 1\%$ of the area of the HI(v,J) peaks that arise from intracluster scattering.

The shape of the $^3\Pi_{0+}$ HI potential, which is the entrance channel for the I* quenching that is referred to as "superelastic scattering," provides a unique opportunity for intracluster scattering. Strong spin–orbit coupling ensures that $^3\Pi_{0+}$ is rather flat, with a rather shallow well, down to small r. Thus, HI photodissociation and subsequent H+I* scattering within the same complex can be treated as reasonably separate events. This accounts for the good agreement between the experimental β peak and the binary collision model presented herein.

ACKNOWLEDGMENT

[1] K. Balasubramanian, *Relativistic Effects in Chemistry, Parts A and B* (Wiley, New York, 1997).
[2] A. B. Alekseyev, H. P. Liebermann, D. B. Kokh, and R. J. Buenker, J. Chem. Phys. **113**, 6174 (2000).
[3] N. Balakrishnan, A. B. Alekseyev, and R. J. Buenker, Chem. Phys. Lett. **341**, 594 (2001).
[4] D. Dai and K. Balasubramanian, J. Chem. Phys. **93**, 1837 (1990).
[5] K. Balasubramanian, J. Chem. Phys. **89**, 5731 (1988).
[6] D. Baugh, B. Koplitz, Z. Xu, and C. Wittig, J. Chem. Phys. **88**, 879 (1988).
[7] B. Koplitz, Z. Xu, and C. Wittig, Appl. Phys. Lett. **52**, 860 (1988).
[8] K. G. Dyall, P. R. Taylor, K. Faegri, and H. Partridge, J. Chem. Phys. **95**, 2583 (1991).
[9] J. Müller and H. Ågren, J. Chem. Phys. **76**, 5060 (1982).
[10] K. Balasubramanian, J. Chem. Phys. **116**, 3568 (2002).
[11] K. Sumathi and K. Balasubramanian, J. Chem. Phys. **92**, 6604 (1990).
[12] K. Balasubramanian, M. Han, and M. Z. Liao, J. Chem. Phys. **86**, 4979 (1987).
[13] J. Underwood, D. Chastaing, S. Lee, P. Boothe, T. C. Flood, and C. Wittig, Chem. Phys. Lett. **362**, 483 (2002).
[14] L. Visscher, J. Styszyñski, and W. C. Nieuwpoort, J. Chem. Phys. **105**, 1987 (1996).
[15] D. A. Chapman, K. Balasubramanian, and S. H. Lin, J. Chem. Phys. **87**, 5325 (1987).
[16] C. Zener, Proc. R. Soc. London, Ser. A **137**, 696 (1932).
[17] E. E. Nikitin, Annu. Rev. Phys. Chem. **50**, 1 (1999).
[18] J. Heinrichs, Phys. Rev. **176**, 141 (1968).
[19] C. Zhu, J. Chem. Phys. **105**, 4159 (1996).
[20] C. Zhu and H. Nakamura, J. Chem. Phys. **101**, 4855 (1994).
[21] C. Zhu and H. Nakamura, J. Chem. Phys. **102**, 7448 (1995).
[22] R. L. Pastel, J. K. McIver, H. C. Miller, and G. D. Hager, J. Chem. Phys. **100**, 3624 (1994).

[23] M. B. Faist and R. B. Bernstein, J. Chem. Phys. **64**, 2971 (1976).

[24] W. R. Thorson, J. B. Delos, and S. A. Boorstein, Phys. Rev. A **4**, 1052 (1971).

[25] G. V. Dubrovskii, Sov. Phys. JETP **19**, 591 (1963).

[26] M. Weissbluth, *Atoms and Molecules* (Academic, New York, 1978).

[27] C. E. Moore, *Atomic Energy Levels* (National Bureau of Standards, Washington, DC, 1971).

[28] E. E. Nikitin, *Theory of Elementary Atomic and Molecular Processes in Gases* (Clarendon, Oxford, 1974).

[29] E. E. Nikitin and S. Y. Umanskii, *Theory of Slow Atomic Collisions* (Springer-Verlag, New York, 1984).

[30] D. R. Bates, Proc. R. Soc. London, Ser. A **257**, 22 (1960).

[31] J. Zhang, M. Dulligan, J. Segall, Y. Wen, and C. Wittig, J. Phys. Chem. **99**, 13680 (1995).

[32] J. B. Marion and S. T. Thornton, *Classical Dynamics of Particles and Systems*, 4th ed. (Saunders College Publishing, Philadelphia, 1995).

[33] R. N. Porter, J. Chem. Phys. **45**, 2284 (1966).

[34] J. Segall, J. Zhang, M. Dulligan, R. A. Beaudet, and C. Wittig, Faraday Discuss. Chem. Soc. **97**, 195 (1994).

[35] A. B. McCoy, Y. Hurwitz, and R. B. Gerber, J. Phys. Chem. **97**, 12516 (1993).

[36] A. T. Pritt and R. D. Coombe, J. Chem. Phys. **65**, 2096 (1976).

[37] J. S. Zhang, M. Dulligan, and C. Wittig, J. Phys. Chem. **99**, 7446 (1995).

[38] T. L. Mazely and M. A. Smith, J. Chem. Phys. **89**, 2048 (1988).

[39] J. F. Ogilvie, Trans. Faraday Soc. **67**, 2205 (1971).

[40] W. Demtröder, *Laser Spectroscopy: Basic Concepts and Instrumentation* (Springer-Verlag, Berlin, 1996).

[41] T. F. Gallagher, *Rydberg Atoms* (Cambridge University Press, Cambridge, New York, 1994).

[42] L. Schnieder, K. Seekamp-Rahn, E. Wrede, and K. H. Welge, J. Chem. Phys. **107**, 6175 (1997).

[43] R. Hilbig and R. Wallenstein, IEEE J. Quantum Electron. **19**, 194 (1983).

[44] D. J. Gendron and J. W. Hepburn, J. Chem. Phys. **109**, 7205 (1998).

[45] H. Lefebvre-Brion and R. W. Field, *Perturbations in the Spectra of Diatomic Molecules* (Academic, Orlando, 1986).

[46] M. P. Allen and D. J. Tildesley, *Computer Simulation of Liquids* (Oxford University Press, New York, 1987).

[47] M. J. Romanelli, in *Mathematical Methods for Digital Computers*, edited by H. S. Wilf (Wiley, New York, 1960), p. 110.

[48] P. M. Aker and J. J. Valentini, J. Phys. Chem. **97**, 2078 (1993).

[49] A. D. Buckingham and P. W. Fowler, J. Mol. Struct. **189**, 203 (1988).

[50] Y. Hannachi and B. Silvi, J. Mol. Struct.: THEOCHEM **59**, 483 (1989).

[51] N. Ohashi and A. S. Pine, J. Chem. Phys. **81**, 73 (1984).

[52] W. Chen, A. R. Hightwalker, S. E. Novick, and F. Tao, J. Chem. Phys. **106**, 6240 (1997).

[53] B. J. Howard, T. R. Dyke, and W. Klemperer, J. Chem. Phys. **81**, 5417 (1984).

[54] K. C. Janda, J. M. Steed, S. E. Novick, and W. Klemperer, J. Chem. Phys. **67**, 5162 (1977).

[55] L.-M. Dubernet and J. M. Hutson, J. Phys. Chem. **98**, 5844 (1994).